The Astrophysical Journal Letters, 917:L38 (10pp), 2021 August 20 https://doi.org/10.3847/2041-8213/ac1ad3

Luminosity Dependence of the Cyclotron Line Energy in 1A 0535+262 Observed by Insight-HXMT during the 2020 Giant Outburst

L. D. Kong[1,2], S. Zhang[1], L. Ji[3], P. Reig[4,5], V. Doroshenko[6,7], A. Santangelo[6], R. Staubert[6], S. N. Zhang[1,2], R. Soria[8,9], Z. Chang[1], Y. P. Chen[1], P. J. Wang[1,2], L. Tao[1], and J. L. Qu[1,2]

[1] Key Laboratory for Particle Astrophysics, Institute of High Energy Physics, Chinese Academy of Sciences, 19B Yuquan Road, Beijing 100049, People's Republic of China; kongld@ihep.ac.cn, szhang@ihep.ac.cn, jilong@mail.sysu.edu.cn
[2] University of Chinese Academy of Sciences, Chinese Academy of Sciences, Beijing 100049, People's Republic of China
[3] School of Physics and Astronomy, Sun Yat-Sen University, Zhuhai, 519082, People's Republic of China
[4] Institute of Astrophysics, Foundation for Research and Technology-Hellas, 71110 Heraklion, Crete, Greece
[5] University of Crete, Physics Department, 70013 Heraklion, Crete, Greece
[6] Institut für Astronomie und Astrophysik, Kepler Center for Astro and Particle Physics, Eberhard Karls, Universität, Sand 1, D-72076 Tübingen, Germany
[7] Space Research Institute of the Russian Academy of Sciences, Profsoyuznaya Str. 84/32, Moscow 117997, Russia
[8] College of Astronomy and Space Sciences, University of the Chinese Academy of Sciences, Beijing 100049, People's Republic of China
[9] Sydney Institute for Astronomy, School of Physics A28, The University of Sydney, Sydney, NSW 2006, Australia
Received 2021 July 9; revised 2021 August 4; accepted 2021 August 5; published 2021 August 24

Abstract

We report on a detailed spectral analysis of the transient X-ray pulsar 1A 0535+262, which underwent the brightest giant outburst ever recorded for this source from 2020 November to December with a peak luminosity of 1.2×10^{38} erg s^{-1}. Thanks to the unprecedented energy coverage and high-cadence observations provided by Insight-HXMT, we were able to find for the first time evidence for a transition of the accretion regime. At high luminosity, above the critical luminosity 6.7×10^{37} erg s^{-1}, the cyclotron absorption line energy anticorrelates with luminosity. Below the critical luminosity, a positive correlation is observed. Therefore, 1A 0535+262 becomes the second source after V0332+53, which clearly shows an anticorrelation above and transition between correlation and anticorrelation around the critical luminosity. The evolution of both the observed CRSF line energy and broadband X-ray continuum spectrum throughout the outburst exhibits significant differences during the rising and fading phases; that is, for a similar luminosity, the spectral parameters take different values, which results in hysteresis patterns for several spectral parameters including the cyclotron line energy. We argue that, similar to V0332+53, these changes might be related to the different geometry of the emission region in rising and declining parts of the outburst, probably due to changes in the accretion disk structure and its interaction with the magnetosphere of the neutron star.

Unified Astronomy Thesaurus concepts: X-ray astronomy (1810); High mass x-ray binary stars (733); Pulsars (1306)

1. Introduction

Accreting pulsars are neutron stars (NSs) with a magnetic field of $B \sim 10^{12}$ G orbiting and powered by accretion from a massive (spectral type late O or early B) companion star (Reig & Nespoli 2013). The strong magnetic field implies a relatively large magnetospheric radius of $\sim 10^{7-10}$ cm. At the magnetosphere, the accreting plasma is forced to follow the magnetic field lines, and matter is channeled mostly onto the magnetic poles (mounds or columns, depending on the luminosity). In the hot, highly magnetized plasma, the kinetic energy of the infalling material is converted to heat and radiation. Typical cutoff power-law continuum spectra and absorption features are generated in these structures.

The magnetic field in many of these objects can be measured directly through measurement of the energies of so-called cyclotron resonant scattering features (CRSFs) modifying the continuum X-ray spectrum of X-ray pulsars. These are characteristic absorption-like features found in the spectra of highly magnetized accreting pulsars, usually from ~10 to 100 keV, corresponding to so-called Landau levels (Staubert et al. 2019) and directly related to field strength in the line-forming region. The centroid line energies $E_{\rm cyc}$ are expected, e.g., at

$$E_{\rm cyc} = \frac{n}{(1+z)}\frac{\hbar e B}{m_{\rm e} c} \approx 11.6\,\frac{n}{(1+z)} \times B_{12}\ ({\rm keV}), \quad (1)$$

where B_{12} is the magnetic field strength in units of 10^{12} G, z is the gravitational redshift due to the NS mass, and n is the number of the Landau level involved, e.g., $n = 1$ for the fundamental line and $n \geqslant 2$ for the harmonics.

With the increase in precision of CRSF measurements, the dependence of CRSFs on luminosity and spin phase has become obvious and is one of the important areas of current X-ray pulsar research, as it potentially allows probing of emission region geometry and properties (Staubert et al. 2019). Of particular interest is the luminosity dependence of the line properties, as it might be used to probe the mechanism of plasma deceleration and the transition between so-called sub- and supercritical accretion regimes associated with the onset of an accretion column first suggested by Basko & Sunyaev (1976). As a result, two main accretion regimes, super- and subcritical accretion, are expected depending on whether the source luminosity is higher or lower than a "critical luminosity" $L_{\rm crit}$, which strongly depends on the magnetic field of the NS (Basko & Sunyaev 1976; Becker et al. 2012; Mushtukov et al. 2015a). In the supercritical regime, for $L > L_{\rm crit}$, an accretion column forms, and the falling plasma is decelerated by a

radiation shock that forms at a certain distance from the NS surface. In this case, the emission height increases with increasing luminosity. In the subcritical regime, for $L < L_{\rm crit}$, the infalling matter is presumably decelerated by Coulomb interaction, forming a region whose height decreases with increasing luminosity. At even lower luminosity, the description of the deceleration process of falling material is not very conclusive. A reasonable scenario is that there exists a transition for the regime from Coulomb-stopping to gas-shock dominance beyond which only a small accretion mound forms on the NS surface. Based on this picture, and considering that the local magnetic field strength decreases with height, the correlation between the CRSF line energy and luminosity can be used to trace the accretion regimes. For instance, a transition between the sub- and supercritical regimes was recently reported by Doroshenko et al. (2017) and Vybornov et al. (2018) for V0332+53 during a giant outburst.

So far, a clear negative correlation between $E_{\rm cyc}$ and the X-ray luminosity was only confirmed in V0332+53 (Makishima et al. 1990; Tsygankov et al. 2010; Cusumano et al. 2016; Doroshenko et al. 2017; Vybornov et al. 2018), while for 4U 0115+63, the reported anticorrelation is debated (Nakajima et al. 2006; Tsygankov et al. 2007; Müller et al. 2013; Iyer et al. 2015). A positive correlation of the line centroid with luminosity is more common, and it has been found in Her X-1 (Staubert et al. 2007), Vela X-1 (Fürst et al. 2014), GX 304-1 (Klochkov et al. 2012), and Cep X-4 (Fürst et al. 2015). For 1A 0535+262, the relationship between cyclotron energy and luminosity is not settled, with some results supporting a positive correlation (Reig & Nespoli 2013; Sartore et al. 2015) and others reporting the absence of any correlation (Terada et al. 2006; Caballero et al. 2007; Klochkov et al. 2011). Objects GX 304-1 and Vela X-1 also appear to show a flattening of the correlation with increasing luminosity (Rothschild et al. 2017; La Parola et al. 2016). Here we investigate the luminosity dependence of the line properties in another Be X-ray binary transient, 1A 0535+262, at luminosities exceeding those reached in previous investigations.

The transient X-ray binary 1A 0535+262 was discovered in outburst during observations of the Crab by the Rotation Modulation Collimator on Ariel V through detection of pulsations with a period of ∼104 s (Rosenberg et al. 1975). The system is composed of an O9.7IIIe donor star and a strongly magnetized NS (Steele et al. 1998). The orbit has an eccentricity of $e = 0.47$ and an orbital period of $P_{\rm orb} \sim 110.3$ days (Finger et al. 1996). The distance to 1A 0535+262 is 2 kpc, which has been recently confirmed by Gaia (Bailer-Jones et al. 2018). The fundamental line and first harmonic have been detected at ∼46 and ∼100 keV by different missions during different outbursts (Kendziorra et al. 1994; Grove et al. 1995; Staubert et al. 2019). A somewhat higher CRSF line energy of ∼50 keV was found during the preoutburst flare that took place about 5 days before the peak of a normal (type I) outburst (Caballero et al. 2008; Postnov et al. 2008).

Since its discovery, 1A 0535+262 has experienced a series of outbursts with peak flux varying from a few hundred mCrab to ∼5.5 Crab (Camero-Arranz et al. 2012; Caballero et al. 2013). After a long period of quiescence following the 2011 outburst, the source went through a giant outburst in 2020 November, with a peak flux recorded as ∼12.5 Crab in the energy range 15–50 keV by Swift/BAT. Owing to the unprecedentedly high intrinsic source flux, observation cadence, and wide energy range covered by Insight-HXMT, we can investigate the following for the first time.

1. The relationship between the CRSF energy and luminosity at a higher luminosity than ever before.
2. The evolution of the spectral parameters during both the rise and decline of the outburst, allowing us to study whether the evolutionary paths are similar or differ (hysteresis) at different phases of the outburst.

Section 2 briefly describes the Insight-HXMT detectors and the data reduction procedure. The details of the spectral analysis are presented in Section 3.1, while Sections 3.2 and 3.3 focus on the evolution of the CRSF with luminosity and time, respectively. Discussion and conclusions are included in Sections 4 and 5.

2. Observation and Data Reduction

The Hard X-ray Modulation Telescope, also dubbed Insight-HXMT (Zhang et al. 2014, 2020), was launched on 2017 June 15 with a science payload that allows observations in a broad energy band (1–250 keV) and with a large effective area at high energies. Insight-HXMT consists of three collimated telescopes, the High Energy X-ray Telescope (HE, 18 cylindrical Na I(Tl)/Cs I(Na) phoswich detectors; Liu et al. 2020), the Medium Energy X-ray Telescope (ME, 1728 Si-PIN detectors; Cao et al. 2020), and the Low Energy X-ray Telescope (LE, swept charge device; Chen et al. 2020), with collecting areas/energy ranges of 5000 $\rm cm^2$/20–250 keV, 952 $\rm cm^2$/5–30 keV, and 384 $\rm cm^2$/1–10 keV and typical fields of view (FoVs) of $1.^\circ6 \times 6^\circ$, $1^\circ \times 4^\circ$ and $1.^\circ1 \times 5.^\circ7$; $5.^\circ7 \times 5.^\circ7$ for LE, ME, and HE, respectively (see Figure 1). Insight-HXMT observed 1A 0535+262 from 2020 November 6 (MJD 59,159) to 2020 December 24 (MJD 59,207), for a total exposure of ∼1.910 Ms. For the analysis reported in this paper, we used the Insight-HXMT Data Analysis Software v2.04, together with the current calibration model v2.05 (http://hxmtweb.ihep.ac.cn/software.jhtml). The data are selected under a series of criteria as recommended by the Insight-HXMT team. In particular, data with an elevation angle larger than 10°, a geometric cutoff rigidity larger than 8 GeV, and an offset for the point position smaller than $0.^\circ04$ were considered. In addition, data taken within 300 s of the South Atlantic Anomaly passage outside of good time intervals identified by onboard software were rejected. Because the Crab (R.A. = 83.63308, decl. = 22.0145) is located close to 1A 0535+262 (R.A. = 84.727396, decl. = 26.315789) and occasionally falls into the FoV of some of the Insight-HXMT detectors, we also exclude the detector boxes, which suffered from contamination by the Crab (see Figure 1).

The energy bands adopted for the spectral analysis are 2–7 keV for the LE, 8–35 keV for the ME, and 30–120 keV for the HE. Because of the uncertain calibration at 22 keV of the ME, we ignore the 20–23 keV range during the spectral analysis for this instrument. The instrumental backgrounds are estimated with the tools provided by the Insight-HXMT team: LEBKGMAP, MEBKGMAP, and HEBKGMAP, version 2.0.9, based on the standard Insight-HXMT background models (Guo et al. 2020; Liao et al. 2020a, 2020b). The XSPEC v12.10.1f software package (Arnaud 1996) was used to perform spectral fitting. In order to improve the counting statistic of the energy spectra, we combined the exposures within 1 day with the *addspec* and *addrmf* tasks. Considering the current accuracy of the instrument calibration, we include

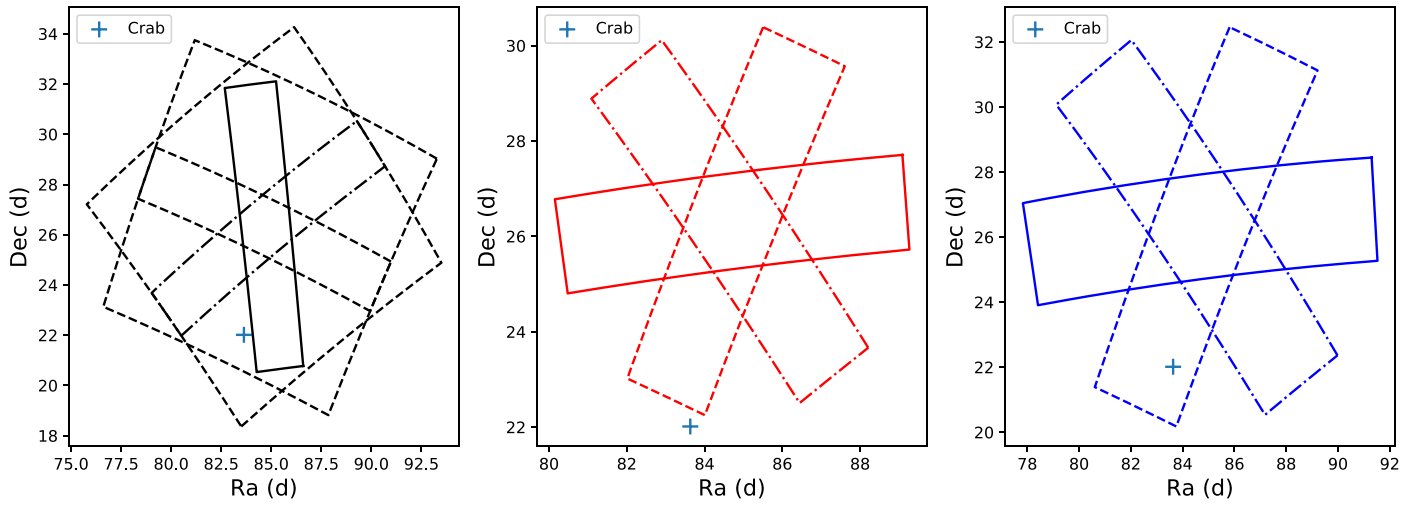

Figure 1. The FoVs for each detector are shown in black for HE (three boxes for small FoVs and two boxes for large FoVs), red for ME, and blue for LE. The blue plus sign shows the Crab's location during ObsID P031431600101.

0.5%, 0.5%, and 1% systematic error for spectral analysis for LE, ME, and HE, respectively. The uncertainties of the spectral parameters are computed using a Markov Chain Monte Carlo (MCMC) with a length of 10,000 and are reported at a 90% confidence level.

3. Results

3.1. The Spectral Analysis

Considering the large number of observations carried out, we only show detailed spectral fits for two representative observations carried out on 2020 November 18 and 2020 December 7. The observation of 2020 November 18 (MJD 59,171) corresponds to the peak of the outburst at a luminosity of 11.67×10^{37} erg s^{-1}, while the X-ray luminosity during the observation on 2020 December 7 (MJD 59,191) was 4.74×10^{37} erg s^{-1} (here and throughout the manuscript, the luminosity is calculated in 2–150 keV, assuming a distance of 2 kpc; Bailer-Jones et al. 2018). In Figure 2, the data from LE, ME, and HE are plotted in black, red, and green, respectively. We first fitted the spectra with the following model: *tbabs* × (*cutoffpl*+*Gaussian*). The *cutoffpl* is a simple continuum with just three free parameters,

$$F(E) = K \times E^{-\Gamma} \exp(-E/E_{\rm fold}), \quad (2)$$

where K, Γ, and $E_{\rm fold}$ determine the normalization coefficient, photon index, and exponential folding energy, respectively. Absorption is taken into account through the *tbabs* model, the Tuebingen–Boulder interstellar medium absorption model (Wilms et al. 2000). The Galactic hydrogen column density toward the pulsar, $n_{\rm H}$, is fixed at 0.59×10^{22} atoms cm^{-2}. The *Gaussian* line is needed to model the iron emission line, usually at $E \sim 6.6$ keV.

Significant residuals at 2–20, ∼45, and ∼100 keV are observed. The residuals at lower energies were accounted for by adding two blackbody components: a hotter one with $kT > 1$ keV and a cooler one with $kT < 1$ keV. The fluxes in 2–10 keV of two blackbodies and *cutoffpl* components are shown in Table 1. Within 2–10 keV, the fluxes of two blackbody components and the *cutoffpl* component were comparable. The absorption features are clearly visible in the residuals of the best-fit spectra with the continuum model described above at ∼45 and ∼100 keV, which is consistent with the previously determined energies of the fundamental CRSF and its harmonic in 1A 0535+262 (Kendziorra et al. 1994; Grove et al. 1995; Staubert et al. 2019), and thus were interpreted as such. To model these lines, we used a multiplicative absorption model *mgabs* with a Gaussian profile,

$$F'(E) = F(E) \times mgabs = F(E) \times \left[\left(1 - \tau_1 e^{\frac{-(E-E{\rm cyc})^2}{2\sigma_1^2}}\right) \times \left(1 - \tau_2 e^{\frac{-(E-R\times E{\rm cyc})^2}{2\sigma_2^2}}\right)\right], \quad (3)$$

where $F'(E)$ is the spectrum modified by *mgabs*, $E_{\rm cyc}$ is the cyclotron line central energy, and τ_1 and σ_1 characterize the central optical depth and the width of the line. The parameter R describes the ratio of the first harmonic line and fundamental line, and τ_2 and σ_2 describe the central optical depth and the width of the first harmonic line.

The model *tbabs* × *magbs* × (*bbodyrad1*+*bbodyrad2*+*Gaussian*+*cutoffpl*) improved the fit considerably, giving a reduced χ^2 of 0.97 and 0.93 for the two observations on 2020 November 18 and December 7, respectively (Table 1). Although some residuals are still present at around 60 keV (Figure 2), these are not significant (F-value = 4.5 and 4.2; see Table 1), and other parameters are not affected by the addition of an extra absorption component. This structure may be caused by the non-Gaussian character of the cyclotron line or the uncertainty of the calibration. Because the significance of this structure is not high, it is difficult to draw any firm conclusion.

The fundamental $E_{\rm cyc}$ was 43 keV during the peak of the outburst and increased to 47 keV during the fading phase of the outburst. The ratio between the fundamental and harmonic line is $R \approx 2.3$, and this ratio is also consistent with the results from INTEGRAL observations (Sartore et al. 2015). The width of the fundamental is about half that of the harmonic, again consistent with previous observations by other satellites, where the width for the fundamental line was measured to be ≈10 and ≈5 keV for the harmonic (Sartore et al. 2015).

The parameters of other spectral components also changed significantly between these two observations. For the observation

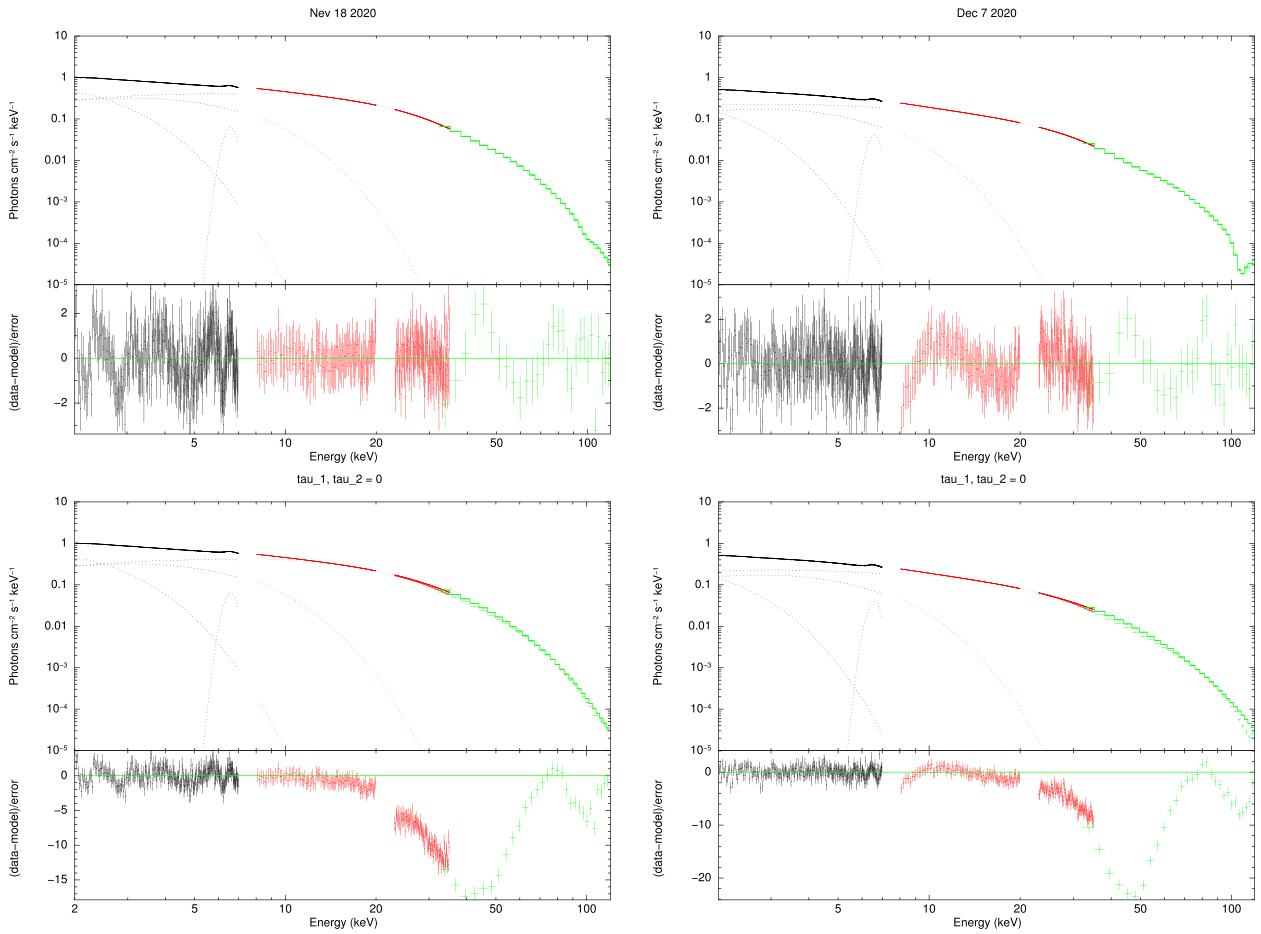

Figure 2. The panels show the spectra and residuals of 2020 November 18 and 2020 December 7. The spectra and residuals from the LE, ME, and HE detectors are shown by black, red, and green points. Two blackbodies, a *cutoffpl*, and an iron emission line are shown in the panels. The residuals without CRSF lines (τ_1, $\tau_2 = 0$) are shown at the bottom of the figure. The parameters are shown in Table 1.

at higher luminosity, the temperatures of the blackbody components are $0.6^{+0.01}_{-0.01}$ and $1.9^{+0.03}_{-0.02}$ keV, higher than those ($0.47^{+0.01}_{-0.01}$ and $1.55^{+0.03}_{-0.01}$ keV) of the observation at lower luminosity. The normalization factors of the blackbody components between the two observations vary from 3999^{+89}_{-224} and 166^{+6}_{-10} to 3151^{+363}_{-300} and 115^{+4}_{-6}.

To study the evolution of the fundamental CRSF line, we initially left all spectral parameters free, except the hydrogen column density that was fixed to 5.9×10^{21} cm^{-2}. Then we also tried fixing R, σ_1, σ_2, and $\sigma_{\rm Fe}$ to the average values 2.3, 10 keV, 5 keV, and 0.3 keV, respectively. Whether these parameters were fixed or not made no significant difference to the other parameters. We will show the details of the spectral evolution in the following sections.

3.2. The CRSF Centroid Energy Evolution

To investigate the evolution of the spectral parameters with time and luminosity, the multicomponent model described in the previous section was fitted to all Insight-HXMT spectra. The left panel of Figure 3 shows the variation of the fundamental line $E_{\rm cyc}$ with L_x (hereafter the luminosity is considered for the 2–150 keV energy range), where the $E_{\rm cyc}$ during the rising and fading phases of the outburst are distinguished by blue and red points. The right panel in Figure 3 shows the outline of the outburst with a resolution of one point per day. The finer sampling of the fading phase allowed us to use a broken linear model to describe the relationship between $E_{\rm cyc}$ and L_x, which is shown with a green line in the left panel of Figure 3. The form of the broken linear model is

$$E_{\rm cyc} = \begin{cases} k_1 \times \left(\dfrac{L_{\rm x}}{10^{37}{\rm erg\ s^{-1}}}\right) + \left(\dfrac{E_0}{1{\rm keV}}\right), & {\rm if}\ \dfrac{L_{\rm x}}{10^{37}{\rm erg\ s^{-1}}} \\ \leqslant \dfrac{L_{\rm break}}{10^{37}{\rm erg\ s^{-1}}} \\ k_2 \times \left(\dfrac{L_{\rm x} - L_{\rm break}}{10^{37}{\rm erg\ s^{-1}}}\right) + k_1 \times \left(\dfrac{L_{\rm break}}{10^{37}{\rm erg\ s^{-1}}}\right) \\ + \left(\dfrac{E_0}{1\ {\rm keV}}\right), & {\rm if}\ \dfrac{L_{\rm x}}{10^{37}{\rm erg\ s^{-1}}} > \dfrac{L_{\rm break}}{10^{37}{\rm erg\ s^{-1}}} \end{cases}, \quad (4)$$

where k_1 and k_2 are the increasing/decreasing rate, and $L_{\rm break}$ is the break point. From the fitting, we get $E_0 = 46.8 \pm 0.14$ keV, $k_1 = -0.04 \pm 0.04$, $k_2 = 0.49 \pm 0.05$, and $L_{\rm break} = 6.7 \pm 0.4$. The $E_{\rm cyc}$ and L_x follow a clear anticorrelation above $L_{\rm break}$, whereas $E_{\rm cyc}$ does not significantly change with L_x below $L_{\rm break}$. Considering that $E_{\rm cyc}$ strongly depends on the magnetic field and the conditions in the region near the NS surface

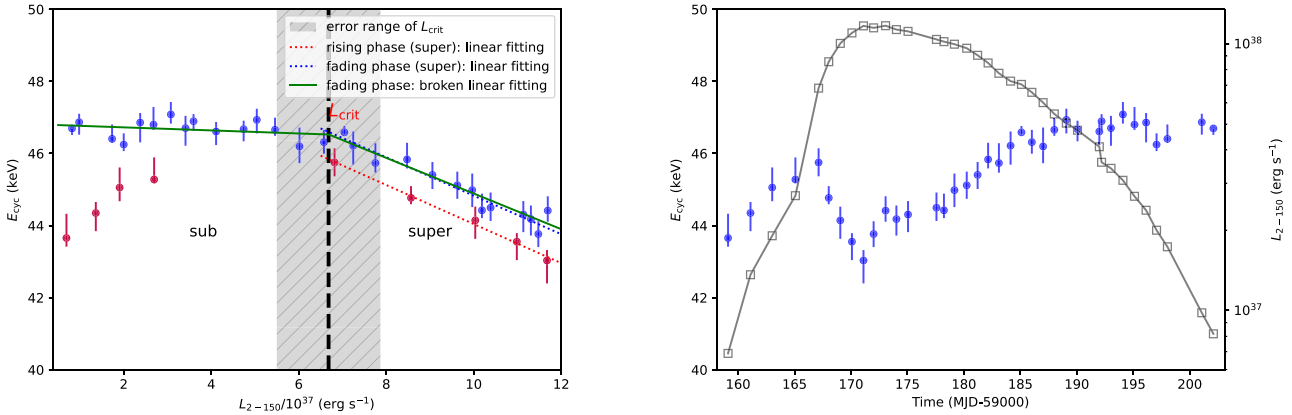

Figure 3. In the left panel, the evolution of E_{cyc} with luminosity is shown. The E_{cyc} in the rising and fading phases are shown in red and blue, respectively. The black dashed line shows the L_{break} with the error range within the gray shadow from a broken linear fitting, which consists of the critical luminosity L_{crit}. The red and blue dotted lines show the fit of the rising and fading trends of E_{cyc} during the supercritical state. In the right panel, the evolution of the fundamental cyclotron line E_{cyc} with time is shown with blue points. The luminosity evolution with time is also shown with black points.

Table 1
Parameters of the Spectral Fitting

Date		2020-11-18			2020-12-07		
MJD		59,171			59,190		
Model	Parameters	2bb+cutoffPL			2bb+cutoffPL		
tbabs	n_H (10^{22} cm^{-2})	0.59 (fixed)	0.59 (fixed)	0.59 (fixed)	0.59 (fixed)	0.59 (fixed)	0.59 (fixed)
gabs	E_{abs} (keV)	⋯	⋯	$59.9^{+7.2}_{-3.9}$	⋯	⋯	$61.0^{+4.8}_{-2.5}$
	σ_{abs} (keV)	⋯	⋯	$3.8^{+2.1}_{-3.3}$	⋯	⋯	$3.3^{+5.6}_{-2.1}$
	τ_{abs}	⋯	⋯	$0.06^{+0.03}_{-0.03}$	⋯	⋯	$0.07^{+0.04}_{-0.05}$
F-test	*F*-value	⋯	⋯	4.5	⋯	⋯	4.2
	P-value	⋯	⋯	0.0035	⋯	⋯	0.0063
mgabs	E_{cyc} (keV)	$43.0^{+0.8}_{-0.4}$	$43.0^{+0.4}_{-0.2}$	$42.4^{+0.8}_{-0.3}$	$47.0^{+1.0}_{-0.2}$	$46.7^{+0.2}_{-0.3}$	$46.2^{+0.6}_{-0.4}$
	σ_1 (keV)	13^{+1}_{1}	10 (fixed)	10 (fixed)	11^{+1}_{1}	10 (fixed)	10 (fixed)
	τ_1	$0.24^{+0.01}_{-0.01}$	$0.18^{+0.01}_{-0.01}$	$0.18^{+0.01}_{-0.01}$	$0.24^{+0.01}_{-0.01}$	$0.24^{+0.01}_{-0.01}$	$0.24^{+0.01}_{-0.01}$
	R	$2.3^{+0.1}_{-0.1}$	2.3 (fixed)	2.3 (fixed)	$2.3^{+0.1}_{-0.1}$	2.3 (fixed)	2.3 (fixed)
	σ_2 (keV)	5^{+3}_{-2}	5 (fixed)	5 (fixed)	8^{+7}_{-2}	5 (fixed)	5 (fixed)
	τ_2	$0.3^{+0.1}_{-0.1}$	$0.3^{+0.1}_{-0.1}$	$0.32^{+0.04}_{-0.02}$	$0.6^{+0.1}_{-0.1}$	$0.8^{+0.2}_{-0.1}$	$0.8^{+0.2}_{-0.1}$
Gaussian	E_{Fe} (keV)	$6.58^{+0.01}_{-0.02}$	$6.59^{+0.02}_{-0.02}$	$6.59^{+0.02}_{-0.01}$	$6.57^{+0.01}_{-0.02}$	$6.58^{+0.02}_{-0.02}$	$6.59^{+0.01}_{-0.01}$
	σ_{Fe} (keV)	$0.19^{+0.02}_{-0.03}$	0.3 (fixed)	0.3 (fixed)	$0.25^{+0.03}_{-0.03}$	0.3 (fixed)	0.3 (fixed)
	Norm (10^{-2})	$3.3^{+0.1}_{-0.3}$	$4.8^{+0.2}_{-0.3}$	$4.7^{+0.3}_{-0.4}$	$2.6^{+0.3}_{-0.3}$	$3.0^{+0.1}_{-0.2}$	$3.0^{+0.3}_{-0.1}$
bbodyrad2	*kT* (keV)	$0.60^{+0.01}_{-0.01}$	$0.56^{+0.01}_{-0.01}$	$0.57^{+0.01}_{-0.01}$	$0.47^{+0.01}_{-0.01}$	$0.44^{+0.02}_{-0.02}$	$0.45^{+0.01}_{-0.02}$
	Norm	3999^{+89}_{-224}	4439^{+276}_{-284}	4348^{+294}_{-171}	3151^{+363}_{-300}	3799^{+666}_{-681}	3625^{+772}_{-173}
	$\log_{10}$(flux) (2–10 keV, erg cm^{-2} s^{-1})	⋯	$-8.63^{+0.03}_{-0.02}$	⋯	⋯	$-9.31^{+0.09}_{-0.04}$	⋯
bbodyrad1	*kT* (keV)	$1.90^{+0.03}_{-0.02}$	$1.70^{+0.03}_{-0.03}$	$1.73^{+0.03}_{-0.03}$	$1.55^{+0.03}_{-0.01}$	$1.50^{+0.02}_{-0.02}$	$1.52^{+0.01}_{-0.03}$
	Norm	166^{+6}_{-10}	175^{+9}_{-8}	173^{+8}_{-8}	115^{+4}_{-6}	123^{+5}_{-8}	122^{+8}_{-3}
	$\log_{10}$(flux) (2–10 keV erg cm^{-2} s^{-1})	⋯	$-7.90^{+0.02}_{-0.02}$	⋯	⋯	$-8.24^{+0.02}_{-0.02}$	⋯
cutoffpl	Γ	$-0.80^{+0.02}_{-0.02}$	$-0.55^{+0.01}_{-0.02}$	$-0.57^{+0.02}_{-0.02}$	$-0.10^{+0.02}_{-0.02}$	$-0.08^{+0.01}_{-0.02}$	$-0.09^{+0.02}_{-0.01}$
	E_{fold}	$9.45^{+0.07}_{-0.04}$	$10.04^{+0.05}_{-0.06}$	$10.01^{+0.05}_{-0.06}$	$12.3^{+0.2}_{-0.1}$	$12.4^{+0.1}_{-0.1}$	$12.4^{+0.1}_{-0.1}$
	K	$0.16^{+0.01}_{-0.01}$	$0.28^{+0.01}_{-0.01}$	$0.26^{+0.01}_{-0.01}$	$0.27^{+0.02}_{-0.01}$	$0.28^{+0.01}_{-0.01}$	$0.28^{+0.02}_{-0.01}$
	$\log_{10}$(flux) (2–10 keV erg cm^{-2} s^{-1})	⋯	$-7.53^{+0.01}_{-0.01}$	⋯	⋯	$-7.84^{+0.01}_{-0.01}$	⋯
Luminosity	$L_{2-150}/10^{37}$ (erg s^{-1})	⋯	$11.67^{+0.03}_{-0.05}$	⋯	⋯	$4.74^{+0.01}_{-0.02}$	⋯
Fitting	χ^2_{red}/d.o.f.	0.97/510	1.03/514	1.01/511	0.93/510	0.95/514	0.93/511

Note. Uncertainties are reported at the 90% confidence interval and were computed using an MCMC of length 10,000. The 0.5%, 0.5%, and 1% system errors for LE, ME, and HE, respectively, have been added during spectral fittings.

where the accretion flow is decelerated, the change in the relationship between E_{cyc} and luminosity points to a change in the accretion regime and allows to tentatively associate the break luminosity with the critical luminosity corresponding to the onset of an accretion column: $L_{break} = L_{crit}/10^{37}$ erg s^{-1} = 6.7 ± 0.4.

Note that there is an important difference in behavior of the line in the rising and declining parts of the outburst, even for comparable luminosities. In particular, there is a positive correlation of $E_{\rm cyc}$ and L_x below $L_{\rm crit}$ during the rising phase, whereas $E_{\rm cyc}$ does not change significantly with luminosity during the fading phase, remaining at ≈47 keV. We note that both types of behavior were not previously reported for 1A 0535+262; however, this is likely to be simply due to the lack of suitable observations. Indeed, Insight-HXMT observations sampled the rising phase of the outburst in detail for the first time, while past investigations of the line properties mostly focused on the declining part of the outburst. This might explain the nondetection of the correlation of the line energy with luminosity at low-to- moderate luminosities up to now. On the other hand, the luminosity range where the anticorrelation is observed was simply not observed previously with instruments capable of accurate measurement of the line energy, since the current outburst of the source is the brightest in recent history.

It is interesting to note also that $E_{\rm cyc}$ is systematically lower during the rising phase than during the fading phase. Within the supercritical zone, the luminosity dependence of the line energy can be fitted by $E_{\rm cyc} = -0.54 \pm 0.03 \times (L_x/10^{37}\,{\rm erg\,s^{-1}}) + 49.5 \pm 0.3$ keV for the rising phase and $E_{\rm cyc} = -0.53 \pm 0.04 \times (L_x/10^{37}\,{\rm erg\,s^{-1}}) + 50.2 \pm 0.4$ keV for the fading phase. Although there is uncertainty in the fit, a shift of 0.7 keV is shown in the left panel of Figure 3, while the slope of the correlation appears to be constant throughout the outburst. We note that this behavior appears to be similar to the line evolution reported by Cusumano et al. (2016), Doroshenko et al. (2017), and Vybornov et al. (2018) for V0332+53, but with some important differences. In particular, in V0332+53, the line energy was (a) lower in the declining phase than in the rising phase of the outburst (i.e., opposite to 1A 0535+262) and (b) consistent with a linear decay in time that resulted in slightly different anticorrelation slopes (Doroshenko et al. 2017).

We emphasize that for both sources, the observed luminosity dependence of the cyclotron line energy is inconsistent with simple predictions of the available theoretical models. Indeed, regardless of the assumed model, the line energy is expected to be related to the height of the column, which in turn is expected to be proportional to the accretion rate, so one expects the same line energy for a fixed luminosity, i.e., no hysteresis, as observed in V0332+53 or 1A 0535+262. Doroshenko et al. (2017) argued that this discrepancy can be resolved if column height is also influenced by additional factors, for instance, magnetospheric radius defining the footprint area of the column and thus indirectly its height. Doroshenko et al. (2017) and Vybornov et al. (2018) demonstrated through analysis of the spin evolution and power spectra of the aperiodic variability that gradual recession of the accretion disk throughout the outburst (for a fixed luminosity) is indeed a plausible explanation for V0332+53. To understand whether a similar scenario can be realized in 1A 0535+262, we also considered the possible complex time and luminosity dependence of the line centroid energy for this source.

In particular, to decouple the time and luminosity dependence of the CRSF energy, we adopted the same approach as Doroshenko et al. (2017) and Vybornov et al. (2018); i.e., we introduced a linear time drift of the centroid energy in addition to the broken linear fit described above. The right panel of Figure 3 shows the time dependence of the X-ray luminosity in 2–150 keV (gray points) and the fundamental CRSF energy (blue points). As a result, we found that an additional linear increase of the line energy at a rate of ∼0.071 keV day^{-1} indeed allows one to describe the overall evolution of the line energy throughout the outburst. We emphasize again that none of the theoretical models predict any hysteresis effects, so our modeling is just an attempt to decouple the theoretically expected luminosity dependence of the line energy from other, as yet unidentified effects. This allows one to discuss them separately and better understand the overall dependence of the line energy.

First of all, we note that after subtracting this linear trend from the observed $E_{\rm cyc} - L_x$ correlation, the transition becomes more prominent, as illustrated in Figure 4. This allows better quantification of the observed properties of this correlation and more accurate measurement of the transition luminosity. We estimate, e.g., slopes for the positive and negative correlation parts at $k_1 = 0.23 \pm 0.05$ and $k_2 = -0.41 \pm 0.04$ with a break at $L_{\rm break} = 6.37 \pm 0.45$. We note that the observed luminosity of the break is consistent with theoretical expectations for the onset of the accretion column (Basko & Sunyaev 1976; Becker et al. 2012; Mushtukov et al. 2015a) and thus interpret the observed transition as the accretion regime transition in 1A 0535+262. Furthermore, the fact that, similarly to V332 +53, the additional time linear drift of the line energy on top of the expected luminosity dependence is required also deserves a discussion.

3.3. Luminosity Dependence of the Broadband Continuum Spectrum

In Figure 5, we plot the evolution of all spectral parameters as a function of luminosity during the outburst. The red and black points represent the rising and fading phases, respectively. The gray dashed line denotes the critical luminosity at 6.7×10^{38} erg s^{-1}. As is evident from the figure, the behavior in the rising and fading phases of the outburst is different for all parameters, with the exception of the τ_1 of the fundamental line. Indeed, although the evolution with X-ray luminosity is smooth, the values of the parameters are significantly different at similar luminosities in the rising and fading phases.

The most prominent changes are seen in the blackbody components at higher luminosity. For both blackbody components, the temperatures are systematically lower in the fading phase, and the normalization parameters evolve in the opposite way. From Figure 5, there is an unexpected hump of ${\rm norm_{b,2}} \sim$ 4000–8000 between 3 and 4×10^{37} erg s^{-1}, and this hump does not match the change of the general trend. At this time, kT_2 evolves into a dip shape. We note that this phenomenon may be caused by the degeneracy between temperature and normalization of the blackbody model, rather than a physical origin. By fixing ${\rm norm_{b,2}}$ at 4000, we find that the evolution of kT_2 becomes smooth and continuous, and other parameters in the model did not change significantly (see blue points in Figure 5). The spectra at low energy, where the blackbody components dominate, also display different trends with luminosity (Figure 5). The normalization of the blackbody is related to the size (radius) of the emitting area as ${\rm norm} = R_{\rm BB}^2/d^2$, where $R_{\rm BB}$ is the radius of the emitting region in kilometers and d is the distance to the source in units of 10 kpc. For a lower-temperature blackbody, the radius size can be limited to $R_{\rm BB} \sim$ 5–13 km, while for a higher-temperature

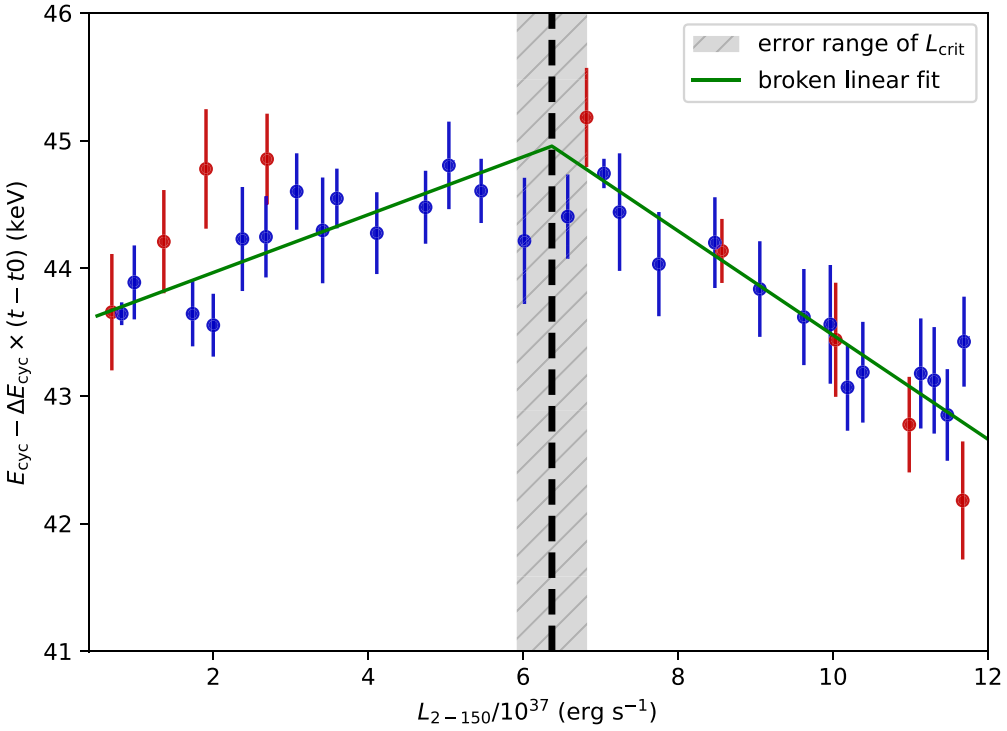

Figure 4. Correlation of the CRSF centroid energy on luminosity with the linear drift of $\Delta E_{cyc} = 0.071$ keV day^{-1} taken into account. The E_{cyc} in the rising and fading phases are shown in red and blue, respectively. The green line shows the broken linear fit. From the fit, the black dashed line shows the transition at 6.37×10^{38} erg s^{-1}. The gray area shows the error range of the transition luminosity.

blackbody, it dominated at a smaller radius size, $R_{BB} \sim$ 1–3 km. The thermal emission radius varies, $R_{BB} \sim 1$–3 km, which appears as a reasonable size for the polar cap. The lower-temperature blackbody could be associated with the top of the column cap (Tao et al. 2019). The asymmetry in the evolution of these two blackbody components throughout the outburst may indicate that the accretion geometry is different in the rising and fading phases.

The spectrum tends to be harder (smaller Γ) and display smaller fold energies in the rising than in the fading phase. We notice that the evolution trends of the spectral parameters in the blackbody and cutoff components do not remain at low luminosity, probably due to the relatively poor statistics of the observational data. The evolution of the harmonic CRSF at $\sim$100 keV (fixed at $2.3 \times E_{cyc}$ for all observations) is not addressed in detail here because of the relatively high HE background at 100 keV and hence a larger systematic uncertainty in precisely measuring the first harmonic CRSF parameter τ_2.

4. Discussion

We have investigated the brightest outburst of 1A 0535+262 observed so far using the data from Insight-HXMT. As a result, we found for the first time a clear anticorrelation between the cyclotron line energy and luminosity above $\sim 6.7 \times 10^{37}$ erg s^{-1} (see Figures 3 and 4). For 1A 0535+262, this trend has not been found in the previous outbursts (Staubert et al. 2019), likely because the luminosity range where it occurs has not been sampled adequately by past observations. This phenomenon is rare, and it has only been seen once before, i.e., in V0332+53 (Makishima et al. 1990; Tsygankov et al. 2010; Cusumano et al. 2016; Doroshenko et al. 2017; Staubert et al. 2019). Thus, 1A 0535+262 is the second source that displays this behavior. We emphasize that our investigation is the first to cover this luminosity range, which explains the nondetection of the anticorrelation by previous studies.

The luminosity dependence of the observed line energy in both regimes has already been extensively discussed in the literature (Tsygankov et al. 2007; Becker et al. 2012; Poutanen et al. 2013; Mushtukov et al. 2015a, 2015b; Staubert et al. 2019). Above the critical luminosity, a higher accretion rate would result in larger radiation pressure and hence a higher accretion column above the magnetic pole and a smaller E_{cyc}, no matter whether the line is observed directly from the column (Tsygankov et al. 2007) or in reflection (Poutanen et al. 2013). In the subcritical regime, the positive correlation between E_{cyc} and L_x can be explained if accreting matter is stopped via the Coulomb braking–dominated process. In this case, a collisionless shock first proposed by Langer & Rappaport (1982) and Bykov & Krasilshchikov (2004) is expected to form at a height inversely proportional to the electron density in the emission region (Shapiro & Salpeter 1975). Therefore, the height of the shock surface decreases with an accretion rate leading to a higher local magnetic field and correlation of the line energy with flux. This model was successfully applied to interpret the E_{cyc}–L_x correlations in Cep X-4 (Vybornov et al. 2017) and GX 304-1 (Rothschild et al. 2017). An alternative explanation for the observed CRSF energy evolution in the subcritical regime is the Doppler effect caused by the radiation pressure, which changes the velocity profile of the falling matter within the line-forming region (Mushtukov et al. 2015b). When the radiation pressure increases with luminosity, the velocity near the NS surface decreases. Consequently, the lower electron velocity results in a smaller redshift and higher CRSF energy. As a result, a positive correlation between the line centroid

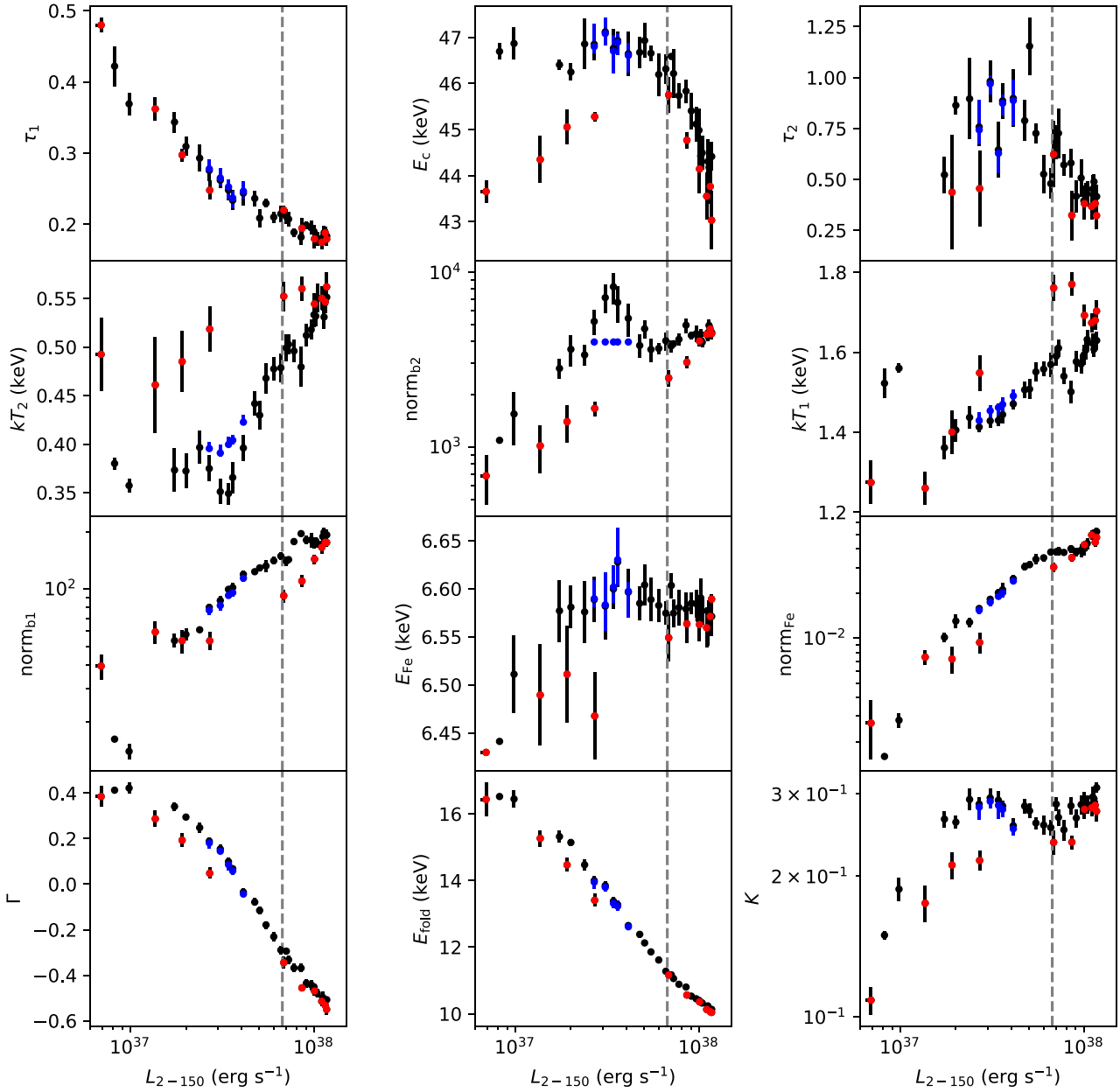

Figure 5. Evolution of all parameters with luminosity L_x. The gray dashed line shows the critical luminosity $L_{\rm crit}$. The rising and fading phases during the outburst are distinguished by red and black points. The blue points show the corrected points by fixing $\mathrm{norm_{b,2}}$ at a reasonable value of 4000.

energy and the luminosity is expected in a regime with subcritical luminosities.

As already mentioned in Section 3.2, however, the observed evolution of the line energy appears to be more complex than the simple predictions outlined above. In particular, it is obvious from Figure 3 that below 6.7×10^{37} erg s^{-1}, the CRSF energy follows two different paths in the rising and fading phases. In the rising phase, $E_{\rm cyc}$ is positively correlated with L_x, while it is approximately constant in the fading phase. We note that past studies of the source in this luminosity range were inconclusive; i.e., some had claimed a positive correlation (Sartore et al. 2015), while others reported the absence of any correlation (Terada et al. 2006; Caballero et al. 2007, 2013). The observed behavior in the current outburst is consistent with these findings, as the source was mostly observed during its outburst decline. The HXMT data confirm the absence of a correlation during the final stages of the outburst.

The overall observed line evolution throughout the outburst can be described as a combination of a time linear increase with a rate of $\Delta E_{\rm cyc} = 0.071$ keV day^{-1} and a broken linear dependence on luminosity shown in Figure 4. This allows us to estimate the transitional luminosity at 6.37×10^{38} erg s^{-1}. We emphasize that this value is only valid under the assumption above, i.e., that the luminosity dependence of the line energy is modified by a time linear drift throughout the outburst. Nevertheless, the obtained value appears to be consistent with the expected critical luminosity value associated with the onset of an accretion column (Basko & Sunyaev 1976; Becker et al. 2012; Mushtukov et al. 2015a), which is estimated to be a broad range of 2.0–6.7×10^{37} erg s^{-1} (Becker et al. 2012;

Mushtukov et al. 2015a). We conclude, therefore, that the observed break in luminosity dependence of the line energy is associated with the transition from the sub- to the supercritical accretion regime.

On the other hand, the origin of the time linear increase of the line energy remains unclear. The asymmetric CRSF behavior was also reported for the 2005 outburst of V0332+53 (Cusumano et al. 2016; Doroshenko et al. 2017); however, the CRSF energy in the rising part of the outburst was larger than in the fading phase in this case. Cusumano et al. (2016) interpreted the observed decrease result as a rapid dissipation of the external magnetic field of the NS due to diamagnetic screening effects caused by accreted matter. Alternatively, Doroshenko et al. (2017) argued that the energy drift of the CRSF was related to the different emission geometries because of different magnetosphere sizes in the rising and fading phases presumably associated with changes in the internal structure of the accretion disk. We emphasize that unlike V0332+53, the time linear drift in 1A 0535 +262 implies an increase rather than a decrease of the line energy with time. This definitively implies that the scenario invoked by Cusumano et al. (2016) cannot be applied in this case and that the observed changes in line energy must be associated with some change of the geometry or intrinsic conditions in the emission region rather any intrinsic field changes.

To qualitatively understand what kind of changes might account for the observed behavior of the line, one could start by adopting the scenario proposed by Doroshenko et al. (2017) for V0332+53 of reversing the rising and declining parts of the outburst, that is, assuming that for some reason, the inner disk radius is larger and the polar cap footprint is smaller during the rising part of the outburst compared to those in the declining part. We emphasize that in this scenario, it is not clear what could lead to the different evolution of the inner disk radius in the two sources, and this discussion is outside the scope of the current work. Therefore, below, we only try to understand whether such a change could, in principle, explain the observed line evolution or whether another explanation needs to be found. With that said, one could anticipate (for a given luminosity) a taller accretion column in the rising phase, which is expected to result in a lower line energy no matter whether the line forms within the accretion column or in the reflection off the NS surface, as proposed by Poutanen et al. (2013). We note that up to now, no other scenarios have been proposed to explain the anticorrelation of line energy with luminosity in the supercritical state, so an assumption that the polar cap indeed has a smaller footprint is, in fact, required in both scenarios to explain the observed increase of the line energy in the supercritical regime in the declining part of the outburst.

Considering that in the case of 1A 0535+262, the hysteresis in line energy is observed for both the sub- and supercritical regimes, it is equally important to also consistently explain the observed increase of the line energy in the subcritical part of the declining part of the outburst. As already mentioned, two scenarios to explain the correlation of line energy with luminosity in the subcritical regime have been proposed in the literature, i.e., a change of the height of the collisionless shock (Langer & Rappaport 1982; Vybornov et al. 2017) and Doppler shifts due to scattering in the accretion flow decelerated by radiative pressure (Mushtukov et al. 2015b). We note that in the latter model, the lower footprint column in the rising phase, which can be characterized in terms of a larger h/d (h is the height above the NS surface, and d is the radius of the hot spot), is actually expected to lead to a lower observed line energy (see, e.g., the lower panel of Figure 2 in Mushtukov et al. 2015b). On the other hand, the larger polar cap size required to explain the higher line energy in the supercritical state in the declining phase of the outburst also implies a lower h/d and higher observed line energy in the subcritical state. We conclude, therefore, that a higher observed line energy (for a given luminosity) in the declining part of the outburst can be qualitatively explained by an increased footprint of the accretion flow. The larger normalization of the blackbody components during the declining phase would agree with this interpretation.

On the other hand, a collisionless shock model with a higher observed line energy in the declining part corresponds to a stronger field in the line-forming region and thus requires a lower shock height resulting in a higher electron density in the scenario considered by Vybornov et al. (2018). Recently, Kulsrud & Sunyaev (2020) proposed that the accretion matter can slip across the magnetic lines under a strong ideal Schwarzschild instability and hence increase the size of the polar cap. This would also imply a lower column height of the collisionless shock, i.e., would also be qualitatively in agreement with observations. We note that an increase of the polar cap size would also be consistent with the scenario by Mushtukov et al. (2015b), i.e., it would be hard to disentangle the two interpretations. On the other hand, leakage of matter through the sides of the column proposed by Kulsrud & Sunyaev (2020) could provide a physical explanation for the increase of the polar cap size in both cases.

We conclude, therefore, that the observed line energy is qualitatively consistent with the assumption of a larger inner disk radius in the rising phase of the outburst. We emphasize, however, that this conclusion is only one possibility, and a detailed quantitative and self-consistent modeling of the observed line energy is required to really understand the behavior of the line in 1A 0535+262 and the differences between this source and V0332+53. Discussion of the latter is beyond the scope of the current outburst; however, we would like to mention that the only obvious difference between the two pulsars is the shorter spin period of V0332+53. This implies that the latter source is likely much closer to corotation during an outburst, which could affect the interaction of the accretion flow with the magnetosphere and potentially alter the magnetosphere's size and the footprint of the accretion column.

5. Conclusions

The high cadence and counting statistics provided by observations of a giant outburst of 1A 0535+262 with Insight-HXMT in a broad energy range revealed for the first time a series of new findings in the context of the variability of the properties of the cyclotron line observed in this source with luminosity and time. First, we were able to detect for the first time a clear anticorrelation of the observed line energy with luminosity above $\sim 6.7 \times 10^{37}$ erg s^{-1}. Furthermore, also for the first time, a clear correlation of the line energy with flux was observed below this luminosity in the rising part of the outburst.

Overall, the observed line energy was found to exhibit complex behavior characterized by the apparent hysteresis of the line parameters between the rising and declining parts of the outburst. This hysteresis can be accounted for by a time linear increase of the line energy at a rate of 0.071 keV day^{-1} on top

of a combination of a correlation with flux below a critical luminosity of $\sim 6.7 \times 10^{37}$ erg s^{-1} and an anticorrelation above this level. This behavior is similar to that previously reported for another Be transient, V0332+53 (Doroshenko et al. 2017; Vybornov et al. 2018), although in the latter case, a time linear decay rather than an increase was observed. The origin of this discrepancy is unclear and a subject for further investigation; however, our results already clearly show that the observed variability of cyclotron lines in X-ray pulsars is clearly more complex than was foreseen by theoretical models.

This work made use of data from the Insight-HXMT mission, a project funded by the China National Space Administration (CNSA) and the Chinese Academy of Sciences (CAS). This work is supported by the National Key R&D Program of China (2016YFA0400800) and the National Natural Science Foundation of China under grants U1838201, 11473027, U1838202, 11733009, U1838104, U1938101, U2038101, and U1938103 and the Guangdong Major Project of Basic and Applied Basic Research (grant No. 2019B030302001).

ORCID iDs

L. D. Kong https://orcid.org/0000-0003-3188-9079
P. Reig https://orcid.org/0000-0002-6446-3050
V. Doroshenko https://orcid.org/0000-0001-8162-1105
A. Santangelo https://orcid.org/0000-0003-4187-9560
R. Staubert https://orcid.org/0000-0003-1498-1543
S. N. Zhang https://orcid.org/0000-0001-5586-1017
R. Soria https://orcid.org/0000-0002-4622-796X
J. L. Qu https://orcid.org/0000-0002-9796-2585

References

Arnaud, K. A. 1996, in ASP Conf. Ser. 101, Astronomical Data Analysis Software and Systems V, ed. V. Systems, G. H. Jacoby, & J. Barnes (San Francisco, CA: ASP), 17
Bailer-Jones, C. A. L., Rybizki, J., Fouesneau, M., Mantelet, G., & Andrae, R. 2018, AJ, 156, 58
Basko, M. M., & Sunyaev, R. A. 1976, MNRAS, 175, 395
Becker, P. A., Klochkov, D., Schönherr, G., et al. 2012, A&A, 544, A123
Bykov, A. M., & Krasilshchikov, A. M. 2004, AstL, 30, 309
Caballero, I., Kretschmar, P., Santangelo, A., et al. 2007, A&A, 465, L21
Caballero, I., Pottschmidt, K., Marcu, D. M., et al. 2013, ApJL, 764, L23
Caballero, I., Santangelo, A., Kretschmar, P., et al. 2008, A&A, 480, L17
Camero-Arranz, A., Finger, M. H., Wilson-Hodge, C. A., et al. 2012, ApJ, 754, 20
Cao, X., Jiang, W., Meng, B., et al. 2020, SCPMA, 63, 249504
Chen, Y., Cui, W., Li, W., et al. 2020, SCPMA, 63, 249505
Cusumano, G., La Parola, V., D'Aì, A., et al. 2016, MNRAS, 460, L99
Doroshenko, V., Tsygankov, S. S., Mushtukov, A. A., et al. 2017, MNRAS, 466, 2143
Finger, M. H., Wilson, R. B., & Harmon, B. A. 1996, ApJ, 459, 288
Fürst, F., Pottschmidt, K., Miyasaka, H., et al. 2015, ApJL, 806, L24
Fürst, F., Pottschmidt, K., Wilms, J., et al. 2014, ApJ, 780, 133
Grove, J. E., Strickman, M. S., Johnson, W. N., et al. 1995, ApJL, 438, L25
Guo, C.-C., Liao, J.-Y., Zhang, S., et al. 2020, arXiv:2003.06260
Iyer, N., Mukherjee, D., Dewangan, G. C., Bhattacharya, D., & Seetha, S. 2015, MNRAS, 454, 741
Kendziorra, E., Kretschmar, P., Pan, H. C., et al. 1994, A&A, 291, L31
Klochkov, D., Doroshenko, V., Santangelo, A., et al. 2012, A&A, 542, L28
Klochkov, D., Staubert, R., Santangelo, A., Rothschild, R. E., & Ferrigno, C. 2011, A&A, 532, A126
Kulsrud, R. M., & Sunyaev, R. 2020, JPlPh, 86, 905860602
La Parola, V., Cusumano, G., Segreto, A., & D'Aì, A. 2016, MNRAS, 463, 185
Langer, S. H., & Rappaport, S. 1982, ApJ, 257, 733
Liao, J.-Y., Zhang, S., Chen, Y., et al. 2020a, arXiv:2004.01432
Liao, J.-Y., Zhang, S., Lu, X.-F., et al. 2020b, arXiv:2005.01661
Liu, C., Zhang, Y., Li, X., et al. 2020, SCPMA, 63, 249503
Makishima, K., Mihara, T., Ishida, M., et al. 1990, ApJL, 365, L59
Müller, S., Ferrigno, C., Kühnel, M., et al. 2013, A&A, 551, A6
Mushtukov, A. A., Suleimanov, V. F., Tsygankov, S. S., & Poutanen, J. 2015a, MNRAS, 447, 1847
Mushtukov, A. A., Tsygankov, S. S., Serber, A. V., Suleimanov, V. F., & Poutanen, J. 2015b, MNRAS, 454, 2714
Nakajima, M., Mihara, T., Makishima, K., & Niko, H. 2006, ApJ, 646, 1125
Postnov, K., Staubert, R., Santangelo, A., et al. 2008, A&A, 480, L21
Poutanen, J., Mushtukov, A. A., Suleimanov, V. F., et al. 2013, ApJ, 777, 115
Reig, P., & Nespoli, E. 2013, A&A, 551, A1
Rosenberg, F. D., Eyles, C. J., Skinner, G. K., & Willmore, A. P. 1975, Natur, 256, 628
Rothschild, R. E., Kühnel, M., Pottschmidt, K., et al. 2017, MNRAS, 466, 2752
Sartore, N., Jourdain, E., & Roques, J. P. 2015, ApJ, 806, 193
Shapiro, S. L., & Salpeter, E. E. 1975, ApJ, 198, 671
Staubert, R., Shakura, N. I., Postnov, K., et al. 2007, A&A, 465, L25
Staubert, R., Trümper, J., Kendziorra, E., et al. 2019, A&A, 622, A61
Steele, I. A., Negueruela, I., Coe, M. J., & Roche, P. 1998, MNRAS, 297, L5
Tao, L., Feng, H., Zhang, S., et al. 2019, ApJ, 873, 19
Terada, Y., Mihara, T., Nakajima, M., et al. 2006, ApJL, 648, L139
Tsygankov, S. S., Lutovinov, A. A., Churazov, E. M., & Sunyaev, R. A. 2007, AstL, 33, 368
Tsygankov, S. S., Lutovinov, A. A., & Serber, A. V. 2010, MNRAS, 401, 1628
Vybornov, V., Doroshenko, V., Staubert, R., & Santangelo, A. 2018, A&A, 610, A88
Vybornov, V., Klochkov, D., Gornostaev, M., et al. 2017, A&A, 601, A126
Wilms, J., Allen, A., & McCray, R. 2000, ApJ, 542, 914
Zhang, S., Lu, F. J., Zhang, S. N., & Li, T. P. 2014, Proc. SPIE, 9144, 914421
Zhang, S.-N., Li, T., Lu, F., et al. 2020, SCPMA, 63, 249502